

Comparison of Image Processing Models in Quark–Gluon Jet Classification

Daeun Kim¹, Jiwon Lee¹, Wonjun Jeong¹, Hyeongwoo Noh¹, Giyeong Kim¹, Jaeyoon Cho¹, Geonhee Kwak¹, Seunghwan Yang¹, and MinJung Kweon^{*1}

¹Department of Physics, Inha University, Incheon, Republic of Korea

Abstract

We present a comprehensive comparison of convolutional and transformer-based models for distinguishing quark and gluon jets using simulated jet images from PYTHIA 8. By encoding jet substructure into a three-channel representation of particle kinematics, we evaluate the performance of convolutional neural networks (CNNs), Vision Transformers (ViTs), and Swin Transformers (Swin-Tiny) under both supervised and self-supervised learning setups. Our results show that fine-tuning only the final two transformer blocks of the Swin-Tiny model achieves the best trade-off between efficiency and accuracy, reaching 81.4% accuracy and an AUC (area under the ROC curve) of 88.9%. Self-supervised pretraining with Momentum Contrast (MoCo) further enhances feature robustness and reduces the number of trainable parameters. These findings highlight the potential of hierarchical attention-based models for jet substructure studies and for domain transfer to real collision data.

1 Introduction

Jets are collimated sprays of hadrons resulting from the fragmentation and hadronization of high-energy quarks or gluons produced in high-energy collisions. At the Large Hadron Collider (LHC), the study of jet substructure provides crucial insights into parton shower dynamics, color coherence, and quark–gluon plasma properties. Since the early 2010s, machine learning has been increasingly used to classify jets based on internal energy flow patterns rather than handcrafted observables [1].

The classification of quark and gluon jets is particularly challenging due to their similar overall shapes and stochastic parton shower processes. However, the difference in color factors — $C_F = 4/3$ for quarks and $C_A = 3$ for gluons — leads to distinct track multiplicities and radiation patterns:

$$\frac{\langle n_{\text{tr}} \rangle_g}{\langle n_{\text{tr}} \rangle_q} \approx \frac{C_A}{C_F} \approx 2.25, \quad (1)$$

where $\langle n_{\text{tr}} \rangle$ denotes the average number of charged particle tracks [2]. These differences manifest in jet images, making them an ideal target for computer vision models.

In this work, we classify quark-gluon jet images using deep learning architectures, including Convolutional Neural Networks (CNNs) and transformer-based models, specifically the Vision Transformer (ViT) and the Shifted Window (Swin) Transformer. While CNNs extract features through the convolution of image kernels with the input data [3], ViT models utilize an attention mechanism to evaluate similarities between image patches, allowing the model to focus on the most relevant features of the data [4]. Owing to this architecture, transformer models have demonstrated strong performance and improved scalability when trained on sufficiently large

*Corresponding author: minjung@inha.ac.kr

datasets. The Swin Transformer further extends this framework by restricting attention to local windows [5] while introducing a hierarchical structure through window shifting and patch merging, allowing the model to capture visual scales of features efficiently [5].

Because transformers typically require large training datasets and computational resources, fine-tuning strategies and model customization are essential, particularly under constrained computational environments. In this study, we employ Momentum Contrast (MoCo), an unsupervised learning framework, to pre-train or modify initial weight parameters. By utilizing a contrastive loss mechanism, MoCo enables the model to extract representative features more efficiently for downstream supervised classification tasks [6].

In this research, we compare the quark–gluon jet classification performance of fine-tuned, pre-trained transformer models against CNN benchmarks, and find that fine-tuning the last two blocks of a Swin Transformer achieves the best overall performance. To improve efficiency, we developed a customized Swin architecture specialized for jet image data and optimized its initial parameters via MoCo pretraining. Our results demonstrate that the custom Swin-MoCo model achieves performance comparable to that of the pre-trained Swin Transformer while significantly reducing the number of trainable parameters and training time. This suggests that transformer models can be effectively adapted for jet classification even in resource-constrained environments. We anticipate that these architectures will be broadly applicable to various other types of High Energy Physics (HEP) data.

This paper is organized as follows. Section 2 describes the quark–gluon jet image dataset used in this analysis. Section 3 introduces the employed machine-learning models, including CNN, ViT, Swin Transformer, and the MoCo framework. Section 4 details the training setup, fine-tuning strategies, and customized Swin architecture. Section 5 presents the classification performance and its dependence on sample size and fine-tuning depth. Finally, Section 6 summarizes our conclusions and discusses future prospects.

2 Dataset

We use the open dataset *Pythia8 Quark and Gluon Jets for Energy Flow* [7], generated at $\sqrt{s} = 14$ TeV and reconstructed with anti- k_T algorithm ($R = 0.4$). In this analysis, the data set is restricted to light-flavor quark jets, explicitly excluding heavy-flavor (charm and bottom) jets. We select jets with transverse momentum $p_T^{\text{jet}} \in [500, 550]$ GeV, and $|y_{\text{jet}}| < 1.7$. Each jet is represented as a 72×72 pixel image in (η, ϕ) space. Examples of the resulting three-channel jet images for quark and gluon jets are shown in Figure 1. Jet substructure information, including jet width and radiation patterns, possesses inherent spatial structure that is preserved through pixelated jet image representation. This approach enables neural networks to automatically learn classification-relevant features without relying on manually designed observables. Furthermore, since jet images follow a standard two-dimensional image representation, we can directly apply computer-vision neural network architectures, including convolutional neural networks (CNNs) and Vision Transformers (ViTs).

We follow the colored jet image procedure proposed in [8], performing jet centering, grid discretization, and normalizing and standardizing the momentum channels (R and G) using their combined p_T scale while leaving the multiplicity channel (b) unnormalized. The image resolution is set to 72×72 pixels, adjusted to suit our analysis environment. The jet images employ a physics-informed multi-channel representation:

- **R-channel:** transverse momenta (p_T) of charged particles;
- **G-channel:** transverse momenta (p_T) of neutral particles;
- **B-channel:** charged particle multiplicity.

This design captures both momentum and multiplicity information, mapping the jet energy flow into a structured visual form suitable for image-based deep learning.



Figure 1: (a) Quark jet and (b) gluon jet. Gluon jets exhibit a broader spatial radiation pattern and higher particle multiplicity compared to quark jets. For visualization purposes, the pixel display size is enlarged relative to the actual input resolution (72×72).

3 Model Architectures

3.1 Convolutional Neural Network (CNN)

Convolutional neural networks (CNNs) extract features by sliding fixed-size convolutional filters across an image and computing features from the pixel patches at each location [3]. Since the output of each neuron depends only on the pixels within the filter’s receptive region, CNNs are structurally most sensitive to correlations between adjacent pixels. This characteristic can be viewed as a locality bias, meaning that CNNs features are constructed primarily from local neighborhoods by design. Due to this structural property, CNNs effectively capture local spatial patterns in jet images by emphasizing correlations among nearby pixels, which aligns well with fine-grained jet substructure cues. In this sense, CNNs are particularly effective at modeling short-range spatial dependencies.

However, the region observable by a single convolutional layer is limited by the filter size. To learn relationships between distant regions—such as between the jet core and outer regions—the network must pass information through multiple convolutional layers, progressively expanding the effective receptive field of higher layers. Moreover, the effective receptive field typically occupies only a fraction of the theoretical receptive field, with pixel contributions concentrated near the center in an approximately Gaussian manner [9]. Yet this process introduces a design trade-off: if the network depth is insufficient or spatial resolution decreases rapidly due to down-sampling at intermediate stages, fine details can be attenuated, making it harder to maintain informative long-range correlations across the entire jet image.

Because jet image classification can involve both local substructure and more global organization of radiation patterns, it is useful to consider architectures that can balance local inductive bias with global context modeling. This locality bias and the way receptive fields expand in CNNs motivate a comparison with Transformer-based models that employ self-attention mechanisms. A Vision Transformer can directly connect any two positions in the entire image through global self-attention, while a Swin Transformer captures correlations over wider ranges through window-based self-attention and shifted-window strategies, enabling more flexible modeling of long-range interactions compared to CNNs.

3.2 Vision Transformer (ViT)

CNNs are strong at capturing short-range patterns, but they have difficulty explicitly modeling long-range interactions [9]. To address this limitation, we consider a self-attention-based Vision Transformer (ViT).

A Vision Transformer represents an image as a sequence of tokens and feeds it into a Transformer encoder [4]. The input image is split into fixed-size patches, and each patch is linearly projected into a patch embedding. For classification tasks, a class token is prepended to the sequence to obtain a representative global representation, and positional embeddings are added to each token to encode spatial location information within the image. The Transformer encoder then applies multiple layers of self-attention blocks to model interactions among tokens.

Let the embedding matrix consisting of N patch tokens be $X \in \mathbb{R}^{N \times d}$, where d is the embedding dimension. For self-attention computation, each token is linearly projected into Query (Q), Key (K), and Value (V) as follows [10]:

$$Q = XW_Q, \quad K = XW_K, \quad V = XW_V, \quad X \in \mathbb{R}^{N \times d}. \quad (2)$$

Transformer self-attention computes token-to-token similarity via the dot product between Query and Key, normalizes it using softmax to obtain attention weights, and updates each token representation by taking a weighted sum of the Value vectors. To mitigate the issue that similarity scores grow with the dimensionality, ViT uses scaled dot-product attention, where d_k denotes the dimensionality of the projected Query/Key vectors:

$$\text{Attention}(Q, K, V) = \text{softmax}\left(\frac{QK^\top}{\sqrt{d_k}}\right)V. \quad (3)$$

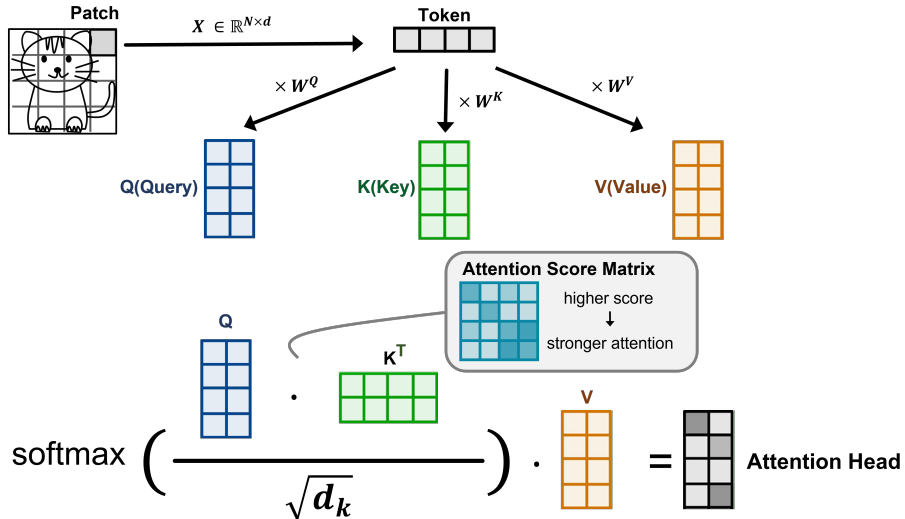


Figure 2: Simplified schematic of the self-attention mechanism. A 4×4 image is split into 2×2 patches, which are projected into Query, Key and Value embeddings. Attention score are computed and applied to obtain the output representation for a single attention head. The class token is omitted for clarity.

A single attention operation estimates relationships within one projection subspace, which can limit expressiveness. To improve representational capacity, ViT employs multi-head attention, generating multiple sets of Q , K , and V with different learned weights. In this setting, the projected Query/Key dimensionality d_k in Eq. (3) corresponds to the per-head dimension d_{head} . Attention is computed in parallel across heads, and the results are concatenated:

$$\text{MultiHead}(X) = [\text{head}_1, \dots, \text{head}_h]W_O. \quad (4)$$

Figure 2 is a schematic illustration of the computational flow of the multi-head self-attention defined in Eqs. (3)-(4). Since each head follows the same computational procedure with different learned weights, the figure presents a representative instance of the per-head attention operation.

Standard ViT uses global self-attention, which can directly model relationships between all pairs of tokens. As a result, it can integrate global information across the entire image from the early stages of learning. These structural properties can be advantageous for jet image classification. In jet images, classification-relevant information is not confined to local pixel-level patterns; it may also involve long-range dependencies such as the relationship between energy distributions in the jet core and outer regions, the global organization of radiation patterns, and correlation structures spanning large radii. This implies that such long-range dependencies can be directly captured via token-to-token attention.

In addition, ViT uses positional embeddings so that token order and spatial location are not lost during attention computation. Given that jet images are constructed on an (η, ϕ) grid, positional embeddings help the model preserve where each token originates in the (η, ϕ) space, enabling it to learn global interactions while still respecting spatial structure. Consequently, ViT can achieve global context-centric representation learning by combining information across multiple spatial scales—such as overall jet width, asymmetry, and radiation patterns—through attention-based aggregation.

3.3 Swin Transformer

CNN-based approaches have been applied to jet-image classification in prior studies [8, 11]. While CNNs effectively capture patterns in neighboring regions through convolution operations, Vision Transformers (ViTs) can directly integrate global information across an image via self-attention [4]. However, a standard ViT may exhibit a relatively weaker inductive bias for learning local patterns. Therefore, in this study, we adopt the Swin Transformer as a practical compromise that preserves the benefit of modeling global interactions while strengthening feature extraction in local regions [5].

The key idea of the Swin Transformer is *window-based attention*, where self-attention is computed locally within non-overlapping windows rather than globally over the entire patch sequence. This design enables efficient learning of local features. In the subsequent block, the windows are shifted to allow cross-window communication, such that progressively broader interactions are incorporated as the blocks are stacked [5].

In addition, the Swin Transformer repeatedly applies a *patch merging* layer that halves the spatial resolution in both height and width, while increasing the embedding dimension. This hierarchical structure learns features at multiple scales instead of processing the input at a single resolution, which is advantageous for forming representations that jointly reflect local details and global context [5]. Accordingly, the Swin Transformer can be considered a meaningful candidate model for jet classification, as it can simultaneously account for local pattern learning and global context integration in jet images.

Figure 3 summarizes the structural differences between ViT and Swin Transformer. Unlike ViT, which relies on global attention with a flat stack of Transformer blocks, Swin employs window-based attention (including shifted windows) and performs patch merging at stage transitions to form a hierarchical multi-scale representation.

3.4 Self-Supervised MoCo Pretraining

To improve learning robustness, we employed Momentum Contrast (MoCo) [6], a self-supervised contrastive learning method, as a pretraining strategy. Transformer-based architectures such as ViT and Swin typically require large-scale datasets to achieve strong performance when trained from scratch [4, 5]. For this reason, pretrained models that have been trained on large natural and object-centric datasets such as ImageNet are commonly adopted to provide

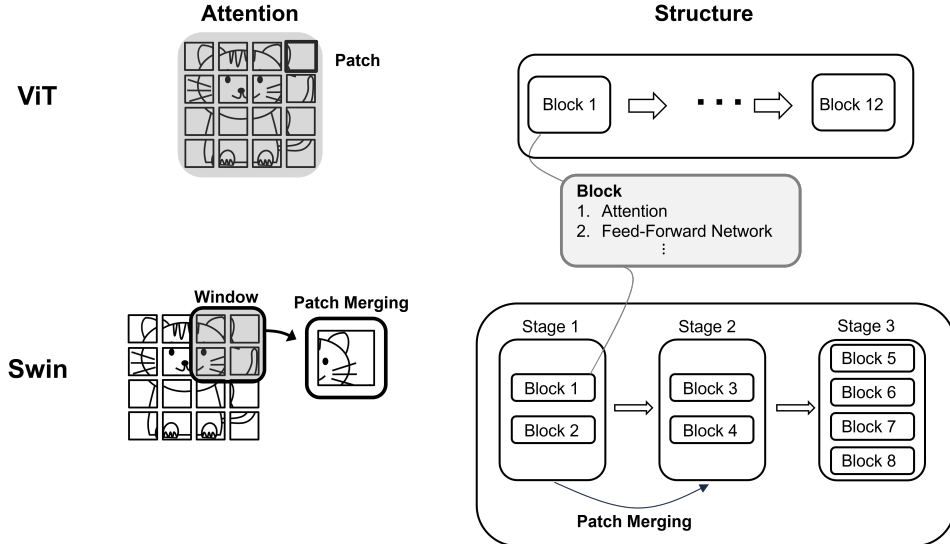


Figure 3: ViT employs global self-attention with a flat stack of Transformer blocks, whereas the Swin Transformer uses window-based local self-attention and shifted windows to enable cross-window interactions. Patch merging between stages further builds a hierarchical multi-scale representation.

robust feature representations. However, since jet images significantly differ from natural images in both structure and semantics, we hypothesize that pretraining on domain-specific jet images can lead to improved performance.

To this end, we adopt Momentum Contrast (MoCo) among various self-supervised pretraining approaches. MoCo is particularly effective at capturing subtle visual differences between highly similar images [6], a property well-suited with the characteristics of jet images, where quark and gluon jets exhibit very similar external structures. By pretraining custom ViT and Swin models using MoCo on our jet image dataset, we aim to overcome the challenges of training transformer-based models from scratch and to improve learning stability by pretraining the models on our data.

MoCo is built upon the concepts of queries and keys, which are used to compare different views of the same image. Given an input jet image, multiple variations are generated, and each resulting view is encoded either as a query or as a key representation. The query represents a reference view, while keys serve as comparison targets in the contrastive learning framework.

When applying variations to jet images, we take into account that jet images are defined in the (η, ϕ) plane [11]. Accordingly, variations excluding rotations and reflections are applied. From these variations, a key k^+ derived from another view of the same original jet image is treated as a positive example, whereas keys k^- originating from different jet images are treated as negative examples.

These query and key representations are processed by an encoder, which extracts feature representations from the input jet images. During training, the encoder is optimized to maximize the similarity between the query q and the positive key k^+ , while minimizing the similarity between the query and negative keys k^- . Through this contrastive learning process, MoCo enables the encoder to learn meaningful representations from jet images, facilitating effective pretraining and improved discrimination between visually similar quark and gluon jets.

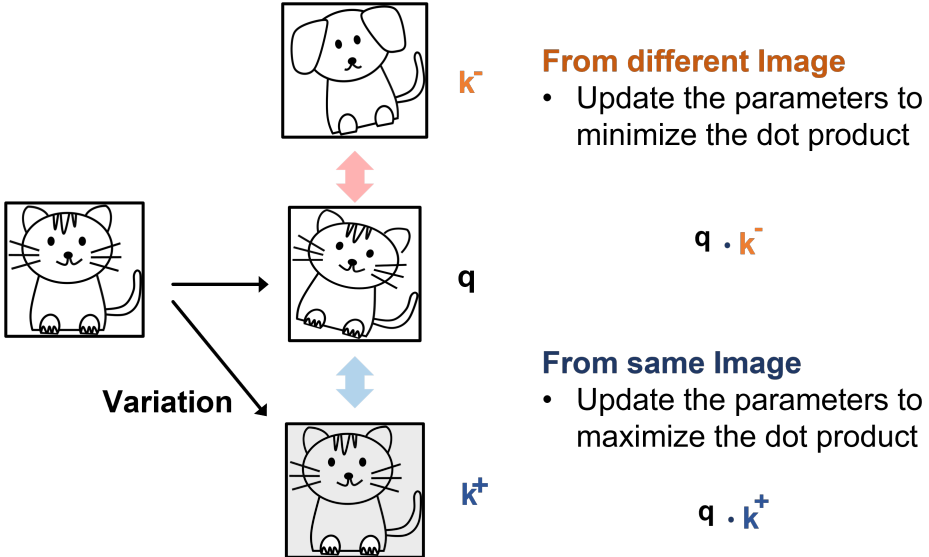


Figure 4: Illustration of the Momentum Contrast (MoCo) framework for jet images. Different views of the same jet image form positive pairs (q, k^+), while views from different images form negative pairs (q, k^-). By maximizing similarity between positive pairs and minimizing similarity to negative pairs, MoCo encourages the encoder to learn discriminative representations for visually similar jet images.

4 Fine-Tuning and Custom Model Strategies

Training setup All models were trained on an NVIDIA RTX 4060 GPU using CUDA on a Windows operating system, with a fixed random seed of 42 to ensure reproducibility. Training was performed for 80 epochs with a batch size of 128, and models were selected based on the best validation ROC-AUC score. For experiments using 20k jet images, the dataset was split into training and validation sets with a ratio of 8:2, while for experiments using 200k jet images, a split ratio of 9:1 was adopted. No data augmentation or additional normalization was applied. For transformer-based models pretrained on ImageNet, input images were upsampled from 72×72 to 224×224 during dataset loading. The model-specific training configurations are summarized in Table 1.

4.1 Fine-Tuning Strategy

Pretrained ViT-Tiny and Swin-Tiny models from the `timm` library [12], which are lightweight variants with reduced model size, originally trained on the ImageNet-1k dataset [4, 5], were fine-tuned on the jet image dataset. Considering training cost and the risk of overfitting, a block-wise fine-tuning strategy was adopted [4, 5], in which only a subset of transformer blocks was unfrozen, allowing the parameters of the unfrozen blocks to be updated during training, while the remaining blocks were kept frozen and their parameters were not updated.

As illustrated in Figure 5, this strategy progressively unfreezes only the final transformer blocks closest to the classification head, while earlier blocks remain frozen [9]. This block-wise fine-tuning scheme is applied identically to both ViT-Tiny and Swin-Tiny models, and the figure provides a schematic representation common to both architectures.

Since the task involves binary classification between quark jets and gluon jets, the classification head was left unfrozen in all configurations to adapt the ImageNet-pretrained 1,000-class output layer to a two-class setting, while the number of unfrozen transformer blocks was varied. Three fine-tuning configurations were explored:

- **0 blocks:** all transformer blocks frozen; only the classification head is trained;

Table 1: Model-specific training configurations, where FT denotes fine-tuning.

Model	Input size	Learning rate	Trainable blocks
CNN	72×72	1×10^{-3}	All layers
Custom Swin	72×72	1×10^{-5}	All layers
Custom Swin + MoCo	72×72	1×10^{-5}	All layers
Swin-Tiny (FT)	224×224	1×10^{-5}	Last 0 / 2 / 4
ViT-Tiny (FT)	224×224	1×10^{-5} (0 blocks: 1×10^{-4})	Last 0 / 2 / 4

- **2 blocks:** the last two transformer blocks unfrozen;
- **4 blocks:** the last four transformer blocks unfrozen.

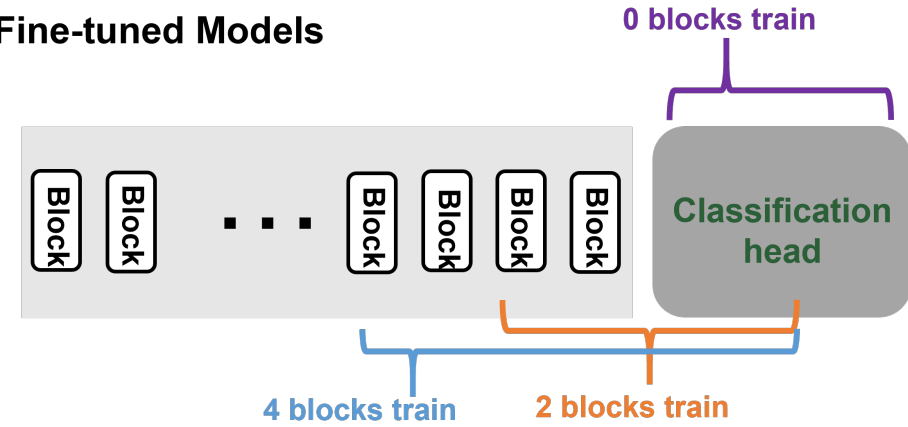


Figure 5: Overview of the block-wise fine-tuning strategy applied to the pretrained ViT-Tiny and Swin-Tiny models. The number of unfrozen transformer blocks is progressively increased from the classification head, while the remaining blocks are kept frozen.

4.2 Custom Swin Model Strategy

Custom models were implemented based on the Swin Transformer architecture, with modifications to the input resolution and model depth to better suit jet image data. Transformer-based models such as ViT and Swin are typically pretrained on natural images with a fixed input resolution of 224×224 [4, 5]. However, jet images are originally defined on a lower-resolution (η, ϕ) grid [11], so using such pretrained models requires upsampling, which introduces redundant pixels that do not contribute meaningful information for model training.

To address this issue, the input resolution was fixed to 72×72 , matching the native resolution of the jet images. This resolution remains sufficient to capture relevant jet substructure information while significantly reducing computational overhead. In addition to the input resolution, the model capacity was adjusted to account for the limited dataset size and the binary nature of the classification task. Transformer-based models with a large number of parameters are more prone to overfitting in low-data regimes. Therefore, a custom Swin architecture was designed with a reduced depth, following the hierarchical design of the original Swin Transformer [5]. After patch embedding with an output dimension of 96, the network is organized into three hierarchical stages. The first, second, and third stages contain 2, 2, and 4 transformer blocks, respectively. As the model progresses through these stages, the feature dimensionality is increased stage by stage from 192 to 384 and finally to 768, while maintaining a patch size of 2 and a window size of 3. As a result of these architectural modifications, the total number

of model parameters was reduced by approximately 86% compared to the original Swin-Tiny architecture, leading to improved training efficiency and reduced overfitting.

Training was conducted on datasets containing 20k and 200k samples using the Adam optimizer.

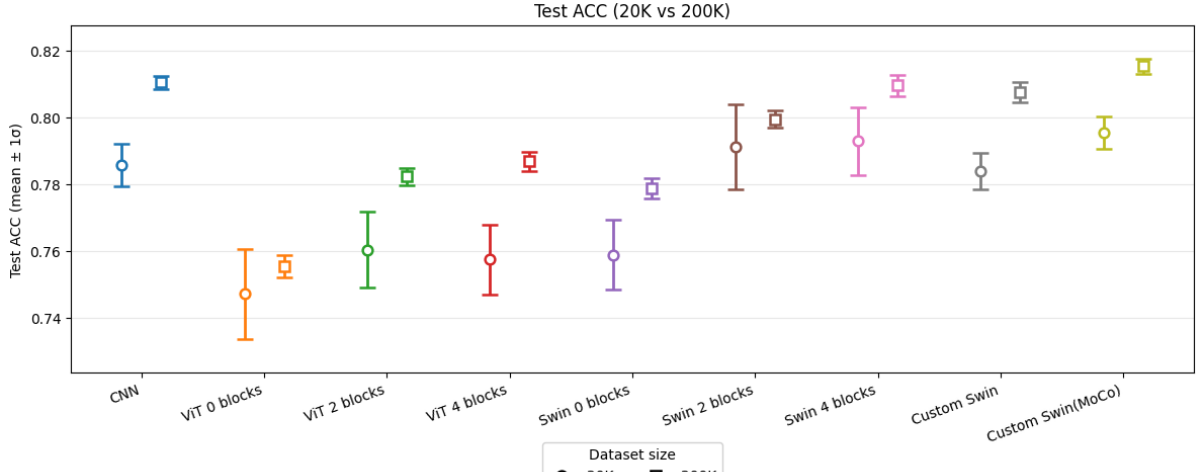
5 Results

Uncertainty from Data Sampling We computed the variation in model performance across multiple independent test sets as follows. For the 20K dataset, the data were split into training and validation sets with an 8:2 ratio (16,000/4,000), and the same ratio was used for the 200K dataset (160,000/40,000). For evaluation, 10 independent test sets were constructed, each having the same size as the corresponding validation set (i.e., 4,000 samples for the 20K dataset and 20,000 samples for the 200K dataset), with no overlap between the training, validation, and test sets. The same test sets were used across all models to ensure a fair comparison. Model performance was averaged over the 10 test sets, and the error bars represent the standard deviation (1σ).

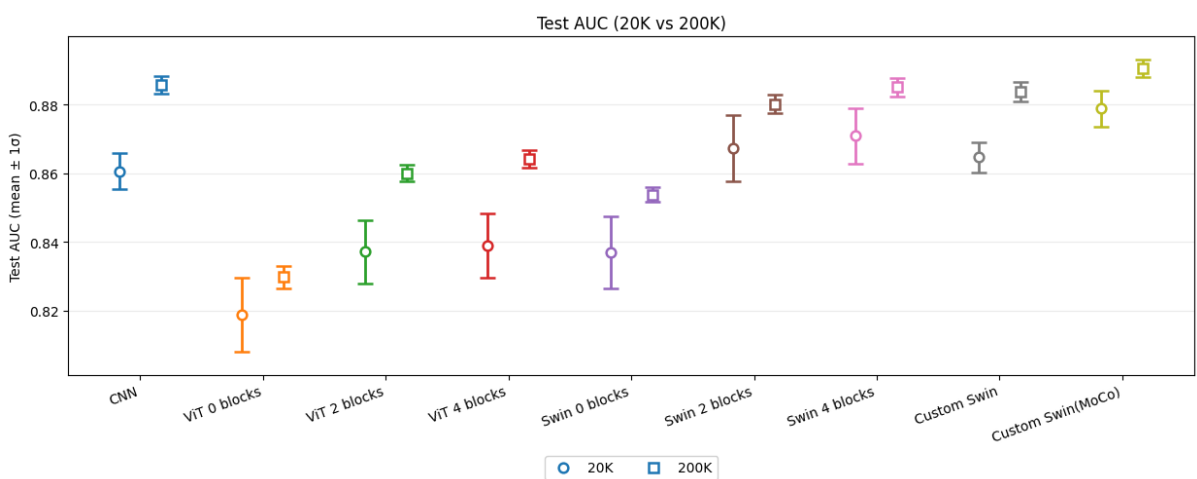
5.1 Performance Comparison Across Models

Figure 6 compares the classification performance of different model architectures. CNN model and Swin Transformers show better performance than ViT models. This can be explained by the fact that CNN-based models and Swin Transformers emphasize local feature extraction, whereas ViT primarily focuses on global representations. These results suggest that jet image classification benefits from considering both localized and global representations, rather than relying on a single perspective that focuses exclusively on either local features or global context.

The custom Swin models, which were introduced to address the limitations of fine-tuned models, demonstrate competitive classification performance. Despite using substantially fewer parameters, the custom models closely follow the performance trends of fine-tuned Swin architectures in both accuracy and AUC. These results show that the observed performance improvements come from overcoming practical limitations of fine-tuned models, such as unnecessary image resizing and additional computation required to match fixed input sizes, as well as the inability to pre-train directly on the target dataset. This suggests that, rather than simply reusing pretrained models as they are, designing models that are better suited to the target data plays an important role in enabling the model to operate efficiently.



(a) ACC



(b) AUC

Figure 6: Test ACC (top) and AUC (bottom) for different model architectures trained on 20K and 200K jet image datasets. Markers indicate mean performance and error bars denote one standard deviation. CNN and Swin Transformers show superior performance compared to ViT models, while custom Swin models achieve comparable results with fewer parameters.

5.2 Training Dynamics and Efficiency

5.2.1 Time-based Validation Analysis (Training Efficiency)

Figure 7 illustrates how different models approach their optimal validation AUC as a function of training time. Among all models, the CNN reaches its peak AUC most rapidly, and the Custom Swin model achieves the highest overall validation AUC.

For the 20K dataset, a clear trend is observed across fine-tuning configurations. As the number of fine-tuned transformer blocks increases, models exhibit faster initial performance gains and reach their peak AUC earlier. However, after achieving the maximum AUC, these models also show a rapid performance degradation. This behavior can be attributed to the increased number of trainable parameters associated with deeper fine-tuning, which leads to overfitting under limited data conditions. Conversely, models with 0-block fine-tuning display much smoother validation AUC curves. While their performance improves more slowly and the peak AUC is relatively lower, these models exhibit stable and gradual performance improve-

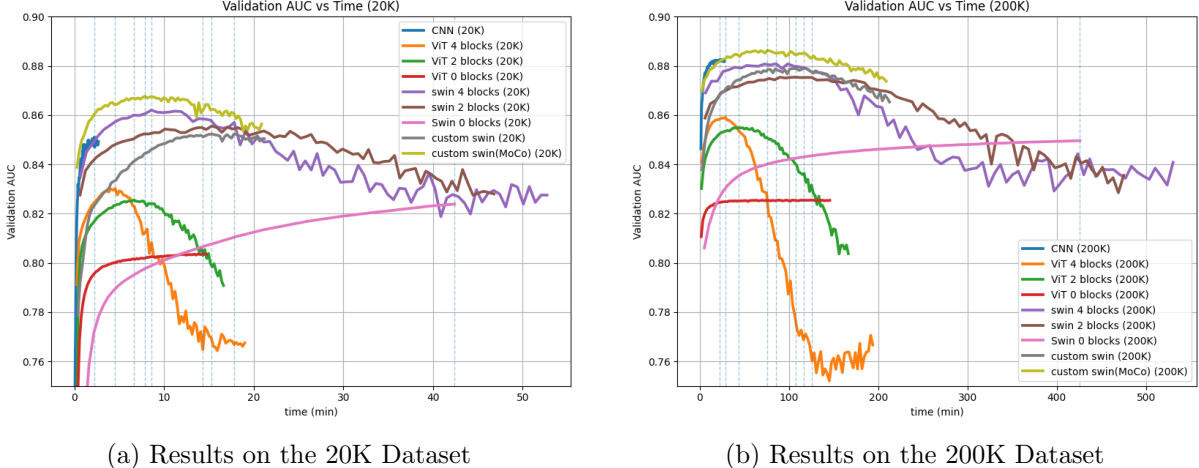


Figure 7: Validation AUC as a function of training time for different model architectures and fine-tuning configurations. Top: results for the 20K dataset; bottom: results for the 200K dataset. Markers indicate the time at which each model achieves its peak validation AUC. Deeper fine-tuning leads to faster initial performance gains but increased instability for smaller datasets, while larger datasets mitigate overfitting and allow sustained performance with deeper fine-tuning.

ments over time without abrupt degradation.

When the dataset size is increased to 200K, the overall behavior changes noticeably. All models achieve higher validation AUC values compared to the 20K case, and the time required to reach the peak AUC generally increases. Due to the larger dataset size, the impact of overfitting is significantly reduced, resulting in a more gradual decline in performance after the peak AUC is reached. As a result, the rate and magnitude of performance degradation become less severe, and models with a larger number of fine-tuned blocks maintain competitive performance for a longer duration.

Taken together, these results highlight an important trade-off between training efficiency and model performance. Models with more aggressively fine-tuned blocks converge more rapidly and achieve higher early performance, but at the cost of increased training time and computational resources, as well as a higher risk of overfitting in data-scarce settings. Conversely, shallower fine-tuning strategies are more computationally efficient and stable, but may limit the achievable peak performance.

These observations suggest that the optimal fine-tuning depth should be chosen by balancing available computational resources, training time, and dataset size. In particular, deeper fine-tuning becomes increasingly beneficial as the dataset size grows, whereas more conservative fine-tuning is preferable when data are limited. Carefully adjusting the fine-tuning strategy according to the data regime is therefore crucial for achieving both efficient training and robust performance.

5.2.2 Epoch-based Validation Analysis (Training Stability)

Figure 8 presents the validation AUC as a function of training epochs. The epoch-based comparison highlights how consistently each model learns as parameter updates accumulate.

For the 20K dataset, a clear instability is observed in models with deeper fine-tuning. Although configurations with a larger number of unfrozen blocks initially achieve rapid AUC improvements, their performance saturates early and subsequently degrades before 40 epochs. This behavior indicates that, under limited data conditions, excessive parameter updates lead to overfitting, leading to worse validation performance even as training continues.

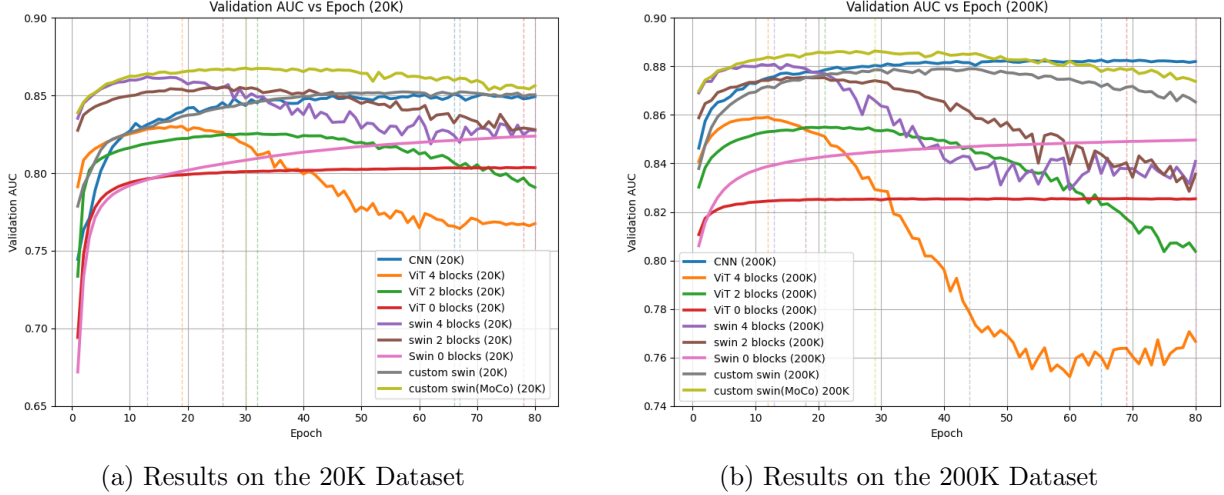


Figure 8: Validation AUC as a function of training epochs for different model architectures and fine-tuning configurations. Top: results for the 20K dataset; bottom: results for the 200K dataset. The figure illustrates differences in learning stability across fine-tuning depths, showing that deeper fine-tuning leads to earlier saturation and stronger performance degradation in low-data regimes, while larger datasets mitigate overfitting effects despite higher model capacity.

In contrast, models with fewer or no fine-tuned blocks exhibit more stable learning dynamics across epochs. In particular, the 0-block fine-tuning configuration shows a smooth and monotonic increase in validation AUC, suggesting that freezing most of the model parameters helps prevent excessive training and avoids sudden performance degradation.

When the dataset size is increased to 200K, validation AUC shows an overall improvement as the number of training epochs increases. However, a different behavior emerges for models with a large number of trainable parameters, such as CNN and transformer models with multiple unfrozen blocks. For these high-capacity models, the performance peak is followed by a steeper decline on an epoch basis in the 200K dataset compared to the 20K case.

This behavior can be attributed to the fact that, as the dataset size increases, each epoch encompasses a larger number of training samples, causing the effects of parameter updates to accumulate more strongly within a single epoch. As a result, when performance is examined on an epoch-by-epoch basis, the post-peak performance degradation can appear more pronounced. Nevertheless, from the perspective of overall training time and model generalization, increasing the dataset size remains effective in mitigating global overfitting.

Overall, larger datasets generally reduce overfitting, epoch-based analyses can make performance degradation appear more rapid for high-capacity models. Therefore, the choice of how many training epochs to use, taking into account the dataset size and model capacity, can significantly influence model performance.

5.2.3 Summary of Training Dynamics

In summary, the results show that the optimal fine-tuning depth depends on both the dataset size and model capacity. Time-based analyses emphasize training efficiency and computational cost, whereas epoch-based analyses provide complementary insights into training stability and overfitting behavior. These observations indicate that model training strategies should be selected with careful consideration of both the data regime and the evaluation perspective.

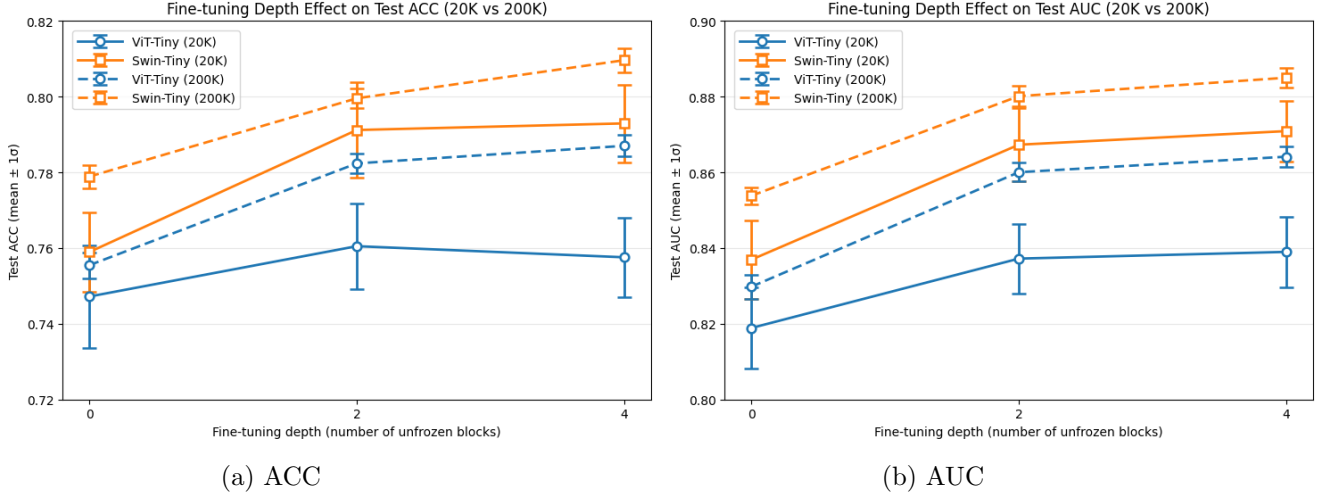


Figure 9: Effect of fine-tuning depth on test accuracy (ACC) and area under the ROC curve (AUC) for ViT-Tiny and Swin-Tiny models. Results are shown for the 20K (solid lines) and 200K (dashed lines) datasets, with error bars indicating one standard deviation. Across both metrics, shallow fine-tuning is sufficient in low-data regimes, while deeper fine-tuning leads to consistent performance improvements as more transformer blocks are unfrozen when sufficient training data are available.

5.3 Effect of Block-wise Fine-tuning

As shown in Figure 9, a clear performance gap between the 20K (solid lines) and 200K (dashed lines) datasets is consistently observed across all fine-tuning depths for both accuracy and AUC. This gap becomes more pronounced as additional transformer blocks are unfrozen, indicating that the effectiveness of deeper fine-tuning strongly depends on the availability of training data.

On the 20K dataset, both ViT-Tiny and Swin-Tiny benefit from fine-tuning up to two blocks, showing moderate improvements in both accuracy and AUC. However, further increasing the fine-tuning depth to four blocks yields only marginal gains and, in some cases, leads to performance degradation. This behavior suggests that under limited data conditions, deeper fine-tuning tends to overfit the training data rather than improving generalization.

In contrast, on the larger 200K dataset, performance consistently improves as the fine-tuning depth increases from two to four blocks for both evaluation metrics. This trend is particularly evident in ViT-Tiny, which exhibits the largest gains in both accuracy and AUC when deeper fine-tuning is applied. These results indicate that sufficient training data enables the model to effectively leverage additional trainable transformer blocks without overfitting.

Overall, the consistent trends observed in both accuracy and AUC demonstrate that the optimal fine-tuning depth is strongly dataset-size dependent. While shallow fine-tuning is preferable in low-data regimes, deeper fine-tuning becomes increasingly beneficial as more labeled data are provided, leading to improved classification performance and more reliable decision boundaries.

5.4 Impact of MoCo Self-supervised Pretraining

Figure 10 shows the impact of MoCo self-supervised pretraining on the performance of the custom Swin models across different dataset sizes.

Overall, models with MoCo pretraining consistently outperform their non-pretrained models. This performance gain can be attributed to MoCo’s ability to learn informative and representations well suited to the task, allowing the model to capture characteristic features of quark and gluon jets.

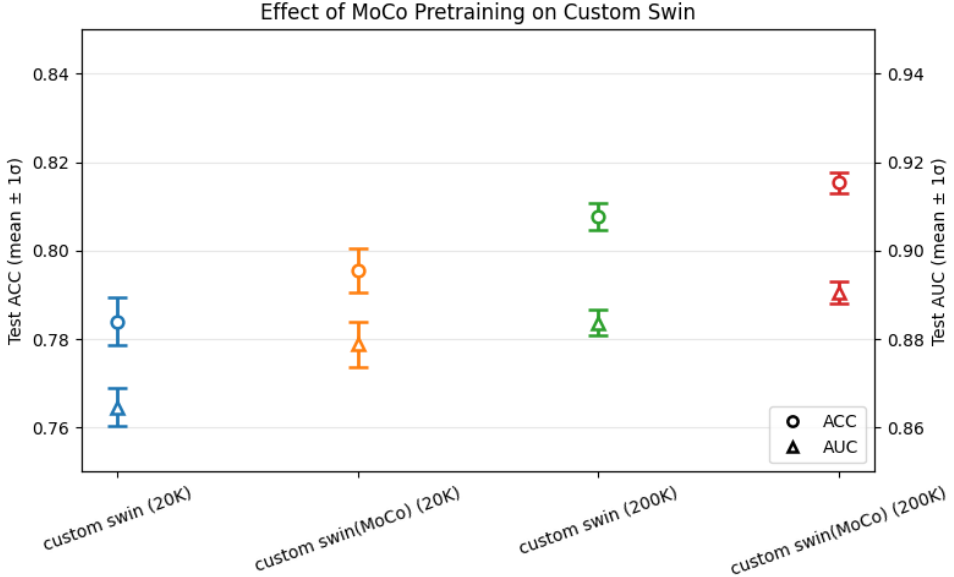


Figure 10: Effect of MoCo self-supervised pretraining on the performance of the custom Swin model. Test accuracy (ACC, circles) and area under the ROC curve (AUC, triangles) are shown for the 20K and 200K datasets, with error bars indicating one standard deviation. MoCo pretraining consistently improves performance across dataset sizes, with particularly strong gains observed in the low-data regime.

As the dataset size increases, both MoCo-pretrained and non-pretrained models show improved performance. However, models trained without MoCo exhibit a larger performance improvement compared to MoCo-pretrained models. This should be interpreted as evidence that MoCo pretraining already captures most of the discriminative features required for quark-gluon classification, resulting in diminishing additional gains from further increases in labeled data. In contrast, non-pretrained models rely more heavily on the number of data samples to learn effective representations, allowing them to gradually catch up as the dataset size increases.

Therefore, MoCo pretraining consistently enhances model performance by facilitating rapid performance improvement during pretraining and enabling the model to effectively learn representations that are well suited to the data. This improvement can be attributed to MoCo’s ability to distinguish visually similar jet images, allowing the model to capture discriminative features that are crucial for quark-gluon classification.

Therefore, employing pretraining plays an important role in effectively training models, and among various pretraining approaches, selecting a method that is well suited to the characteristics of the target data has a significant impact on overall model performance.

6 Discussion and Outlook

We discuss the physical and algorithmic implications of our results and outline directions for future studies.

The superior performance of the Swin-Tiny model can be attributed to its shifted window attention mechanism, which enables the integration of both local jet substructure and global event topology. This property is particularly important for distinguishing soft, isotropic gluon jets from the narrower and more collimated quark jets. Moreover, the hierarchical feature maps learned by Swin are analogous to multi-scale representations of energy flow, which are known to be highly discriminative in jet substructure analyses.

Attention map visualizations further support this interpretation. The early layers predomi-

nantly focus on localized energy deposits, while deeper layers capture broader jet contours and global radiation patterns. These behaviors are consistent with QCD expectations that gluon jets exhibit more isotropic and diffuse energy distributions than quark jets, indicating that the transformer attention mechanism encodes physically meaningful information rather than spurious correlations.

Self-supervised pretraining with Momentum Contrast (MoCo) significantly enhances model robustness by learning contrastive representations across large ensembles of jet pairs. Even when the amount of labeled data is reduced, the pretrained encoder maintains stable classification performance, highlighting its potential for application to real collision data where labels may be uncertain or unavailable.

We also observe that fine-tuning an intermediate number of transformer blocks yields the best performance, whereas unfreezing additional blocks does not provide further gains and can even degrade the results. In particular, the configuration with four unfrozen blocks performs worse than the two-block setting, demonstrating that increasing the number of trainable parameters alone is insufficient to improve generalization. This trend reflects the high parameterization of transformer architectures, which typically require extremely large training datasets to fully benefit from increased model capacity. Even with 200k training samples, excessive fine-tuning appears to drive the model toward over-specialization rather than robust feature learning. In contrast, selectively fine-tuning only the upper transformer layers enables effective task adaptation while preserving pretrained representations, leading to superior generalization.

Looking ahead, several directions can further extend this work. Adaptive fine-tuning strategies, such as block-wise unfreezing and layer-wise learning-rate schedules, may improve stability and performance. Domain adaptation to real LHC collision data will be essential to evaluate robustness against detector effects and simulation mismodeling. Finally, correlating attention heatmaps with physical jet observables, such as jet broadening, multiplicity, and transverse momentum dispersion, will enhance interpretability and strengthen the connection between deep learning representations and QCD dynamics. These developments pave the way for physically interpretable and scalable deep learning approaches to jet substructure studies and QCD modeling.

Acknowledgments

This work was supported by the National Research Foundation of Korea (NRF) under Grant Nos. RS-2008-NR007226 and RS-2025-00559626. The authors acknowledge the open dataset provided by Zenodo and the computational resources of the Inha Physics AI Laboratory.

Appendix

Detailed numerical results for all models are provided in Table 2.

Table 2: Test performance of all models. Results are reported as mean \pm one standard deviation over multiple runs and ft0 indicates fine-tuning with zero trainable transformer blocks.

Model	Test AUC (mean \pm 1 σ)	Test ACC (mean \pm 1 σ)	Test Loss (mean \pm 1 σ)
CNN (20K)	0.8606 \pm 0.0053	0.7857 \pm 0.0064	1.3300 \pm 0.3445
CNN (200K)	0.8857 \pm 0.0026	0.8105 \pm 0.0020	0.4595 \pm 0.0205
ViT ft0 (20K)	0.8189 \pm 0.0107	0.7472 \pm 0.0136	0.5225 \pm 0.0133
ViT ft0 (200K)	0.8298 \pm 0.0032	0.7555 \pm 0.0034	0.5089 \pm 0.0041
ViT ft2 (20K)	0.8372 \pm 0.0092	0.7605 \pm 0.0113	0.5005 \pm 0.0132
ViT ft2 (200K)	0.8600 \pm 0.0025	0.7824 \pm 0.0027	0.4661 \pm 0.0040
ViT ft4 (20K)	0.8390 \pm 0.0093	0.7576 \pm 0.0105	0.5025 \pm 0.0131
ViT ft4 (200K)	0.8641 \pm 0.0026	0.7870 \pm 0.0029	0.4600 \pm 0.0044
Swin ft0 (20K)	0.8369 \pm 0.0105	0.7589 \pm 0.0104	0.5026 \pm 0.0129
Swin ft0 (200K)	0.8538 \pm 0.0022	0.7789 \pm 0.0031	0.4774 \pm 0.0033
Swin ft2 (20K)	0.8673 \pm 0.0096	0.7912 \pm 0.0127	0.4579 \pm 0.0171
Swin ft2 (200K)	0.8801 \pm 0.0027	0.7996 \pm 0.0025	0.4464 \pm 0.0050
Swin ft4 (20K)	0.8709 \pm 0.0081	0.7929 \pm 0.0103	0.4492 \pm 0.0130
Swin ft4 (200K)	0.8850 \pm 0.0027	0.8096 \pm 0.0031	0.4272 \pm 0.0048
Custom Swin (20K)	0.8646 \pm 0.0043	0.7840 \pm 0.0055	0.4763 \pm 0.0084
Custom Swin (200K)	0.8837 \pm 0.0028	0.8077 \pm 0.0030	0.4352 \pm 0.0056
Custom Swin + MoCo (20K)	0.8788 \pm 0.0051	0.7955 \pm 0.0049	0.4496 \pm 0.0099
Custom Swin + MoCo (200K)	0.8905 \pm 0.0025	0.8154 \pm 0.0023	0.4194 \pm 0.0048

References

- [1] A. Larkoski, I. Moult, and B. Nachman, “Jet Substructure at the Large Hadron Collider: A Review of Recent Advances,” *JHEP* 09 (2017) 083.
- [2] Ibid.
- [3] Y. LeCun, B. Boser, J. S. Denker, D. Henderson, R. E. Howard, W. Hubbard, and L. D. Jackel, “Backpropagation Applied to Handwritten Zip Code Recognition,” *Neural Computation* (1989).
- [4] A. Dosovitskiy *et al.*, “An Image is Worth 16x16 Words: Transformers for Image Recognition at Scale,” *ICLR* (2021).
- [5] Z. Liu *et al.*, “Swin Transformer: Hierarchical Vision Transformer using Shifted Windows,” *ICCV* (2021).
- [6] K. He, H. Fan, Y. Wu, S. Xie, and R. Girshick, “Momentum Contrast for Unsupervised Visual Representation Learning,” *CVPR* (2020).
- [7] *Pythia8 Quark and Gluon Jets for Energy Flow*, Zenodo (2019), <https://zenodo.org/record/3164691>.
- [8] P. T. Komiske, E. M. Metodiev, and M. D. Schwartz, “Deep learning in color: towards automated quark/gluon jet discrimination,” *JHEP* 01 (2017) 110, arXiv:1612.01551.
- [9] W. Luo, Y. Li, R. Urtasun, and R. Zemel, “Understanding the Effective Receptive Field in Deep Convolutional Neural Networks,” *Advances in Neural Information Processing Systems* (2016).
- [10] A. Vaswani, N. Shazeer, N. Parmar, J. Uszkoreit, L. Jones, A. N. Gomez, L. Kaiser, and I. Polosukhin, “Attention Is All You Need,” *Advances in Neural Information Processing Systems* (2017).
- [11] L. de Oliveira, M. Kagan, L. Mackey, B. Nachman, and A. Schwartzman, “Jet-Images — Deep Learning Edition,” *JHEP* (2016).

[12] *PyTorch Image Models (timm)*, GitHub repository, <https://github.com/huggingface/pytorch-image-models>.